Assiut University Journal of Multidisciplinary Scientific Research (AUNJMSR)
Faculty of Science, Assiut University, Assiut, Egypt.
Printed ISSN 2812-5029
Online ISSN 2812-5037
Vol. 53(2): 308- 334 (2024)
https://aunj.journals.ekb.eg

One-step hydrothermal synthesis of 2H-MoS_2 nanoflowers for efficient degradation of methylene blue and rhodamine B dyes under UV and visible-light irradiation: A comparative study

Abdulaziz Abu El-Fadl[1,2], A. S. Soltan[1], A. A. Abu-Sehly[1, 2] and M. A. M. Hussien[*1,2]

[1]Physics Department, Faculty of Science, Assiut University, 71516 Assiut, Egypt
[2]Lab. of Smart Materials for Energy Futures, Faculty of Science, Assiut University, 71516 Assiut, Egypt
[*]Corresponding Author: Mahmoud Hussien; email: physicistmahmoud@aun.edu.eg

ARTICLE INFO
Article History:
Received: 2024-03-13
Accepted: 2024-04-21
Online: 2024-04-29

Keywords:
MoS_2,
Hydrothermal method,
Photocatalysis,
Methylene blue,
Rhodamine B,
UV-visible-light

ABSTRACT

Molybdenum disulfide (MoS_2), with its low energy bandgap, plays an essential role in removing organic pollutants from wastewater via the mechanism of photocatalysis. In this paper, the 2H phase of MoS_2 nanoflowers (NFs) as a photocatalyst was synthesized by the facial one-step hydrothermal method. Various characterization techniques, such as X-ray diffraction (XRD), field-emission scanning electron microscopy (FE-SEM), Fourier transform infrared spectroscopy (FT-IR), energy dispersive X-ray spectroscopy (EDX), and UV-visible spectroscopy, were carried out to investigate the structural, morphological, chemical compositional, and optical properties of MoS_2 NFs. The obtained MoS_2 NFs have excellent crystallinity with an average grain size of 6.84 nm. The calculated optical bandgap (E_g) of the MoS_2 NFs was determined to be 1.82 eV. The photocatalytic activity of the as-prepared MoS_2 NFs has been demonstrated by degrading both rhodamine B (RhB) and methylene blue (MB) dyes under ultraviolet (UV) and visible-light irradiation. The results reflected that in the case of using the UV source, the photocatalytic degradation speed of the MB dye is very close to that of the RhB dye, while the degradation of the RhB dye is still faster and more efficient, especially in the first 20 minutes of the irradiation period. However, in the case of using visible light, the MB dye degraded faster and more efficiently than the RhB dye. In addition, the photocatalytic mechanism has been explained, and MoS_2 NFs have shown excellent reusability.

1. INTRODUCTION

In the last few years, the issue of water pollution has emerged as a significant worry for the survival of both humans and the natural environment [1]. The rise in industrial development has resulted in the discharge of untreated, dangerous organic

contaminants directly into bodies of water (such as rivers, ponds, etc.), impacting both the quality level of water and the existence of aquatic organisms [2-4]. Hence, the identification of harmful substances (such as organic pollutants, nitro explosives, heavy metal ions, and others) and the elimination of organic compounds when exposed to light have immense importance in improving the ecosystem [5-7]. Several methods, such as oxidation, carbon filtering, microbial control, membrane filtration, reverse osmosis, phase separation, adsorption, photocatalysis, and others, have been utilized to treat wastewater [8-10]. The process of photocatalysis has been thoroughly studied due to its wide range of environmental uses, such as the production of hydrogen, the degradation of organic compounds, the removal of pharmaceutical waste, the degradation of dyes, and because it is sustainable, eco-friendly, and cost-effective [11-14]. Typically, metallic compounds like titanium dioxide (TiO_2), zinc oxide (ZnO), tin oxide (SnO_2), and others are used as photocatalysts due to their exceptional durability, effective photochemical properties, economical manufacturing, and non-harmful characteristics [15-17]. Although metal oxides have exceptional characteristics, one important aspect to note is their bandgap, which exists within the UV region [16]. Hence, there is a continual quest for substitutes for metal oxides because of their limited range of wavelengths that can activate them, specifically the UV region, which makes up merely 5% of natural sunlight. This necessitates the exploration of alternative options.

Over the past few decades, researchers have shown a high level of intrigue and interest in the field of environmental advancement with regard to semiconductor nanomaterials. These innovative materials have sparked considerable attention, especially when they are used for water purification, due to their exceptional characteristics, such as remarkable physical and chemical properties, minimal harm to living organisms, strong resistance to electrochemical processes, unique dimensions, and expansive surface coverage. Currently, transition metal dichalcogenides (TMDs), with their structural similarity to graphene, have sparked significant attention because of their structural, electronic, optical, and mechanical characteristics. Particularly, the electronic, catalytic, and resistance to photo-corrosion properties of these materials make them well-suited for numerous applications, including energy preservation and transformation, catalysis, and lubrication [18]. These unique characteristics are related to its fundamental layered structure. MX_2 is the general formula for TMDs, where M represents a transition metal element from group IV (Ti, Zr, or Hf), group V (V, Nb, or Ta), or group VI (Mo or W) in the periodic table, and X represents a chalcogen element from group VI (S, Se, or Te) [19, 20].

Layered MoS_2 is one of the most extensively researched TMD systems. The structural arrangement of MoS_2 in two dimensions (2D) exhibits remarkable electrical and optical characteristics with enhanced surface area. The MoS_2 nanoparticles have the potential to be utilized in various fields such as photocatalysis, optoelectronic devices, supercapacitors, photo-detectors, electrocatalysis, batteries, gas sensing, and transistors [17, 21-39]. The existence of MoS_2 is widely known to occur in two distinct crystallographic forms: the trigonal prismatic (2H) phase, which is thermodynamically

stable with a space group denoted as *$P6_3/mmc$* [40], and the octahedral (1T) phase, which is metastable and has a space group designated as *P3m1* [41]. The crystal structure of MoS_2 NFs comprises of strong interlayer covalent bonds between molybdenum (Mo) and sulfur (S) atoms in the trigonal prismatic, with one atomic plane of Mo sandwiched between two atomic planes of S [42]. These layers are connected to each other with weak Van der Waals forces [43].

In spite of its structural similarity to graphene, MoS_2 exhibits unique semiconducting characteristics. In particular, the monolayer form of it possesses an energy bandgap of ~1.9 eV, which is considered a direct bandgap. In contrast, the bulk form of MoS_2 has an energy bandgap of 1.3 eV, which is classified as an indirect bandgap. This is in stark contrast to graphene, which does not possess any bandgaps [44]. This change from an indirect to a direct bandgap is caused by the quantum confinement effect. Due to its bandgap, MoS_2 exhibits photoluminescence, making it an active photocatalyst in the visible light region. The as-prepared MoS_2 nanoparticles have exhibited impressive ability to photodegrade organic dyes because of several active edge locations, a high surface-to-volume ratio, and low energy bandgap.

MoS_2 nanoparticles can be synthesized by various techniques, such as the mechanical exfoliation method, liquid exfoliation method [45, 46], chemical vapor deposition (CVD) method [47-49], sulfurization method [50], and hydrothermal method [48, 51, 52]. However, the hydrothermal method is still one of the most effective methods for growing MoS_2 because it allows for the growth of various morphologies and the exposure of rich edge states [53, 54].

In this work, pure MoS_2 NFs were prepared via a straightforward and effective hydrothermal route without using any surfactant or heat treatment and investigated with different characterization techniques. The MB and RhB dyes are degraded through photocatalysis using MoS_2 NFs photocatalyst under the illumination of two different light sources: ultraviolet (UV) and visible light. This research demonstrates, in a comparative way, the potential of MoS_2 as a versatile and effective photocatalyst against different dyes for environmental remediation. This provides empirical evidence that the photocatalytic activity of MoS_2 NFs depends on the wavelength of the light source (UV or visible) while keeping all the other experimental factors constant, such as the type and concentration of pollutant, amount of catalyst, intensity of the light source, and illumination exposure duration through the experiment.

2. MATERIALS AND METHODS

2.1 Materials

All the chemicals used in these experiments were obtained from the ALPHA CHEMIKA company and utilized without any additional purification. Ultrapure distilled water was used throughout the whole experiment. Ammonium molybdate tetrahydrate ($(NH_4)_6Mo_7O_{24}\cdot 4H_2O$) was used as a source of Mo, and thiourea (CH_4N_2S) was used as a source of S. Two dyes were used in the photocatalysis experiments: MB dye

($C_{16}H_{18}ClN_3S$) and RhB dye ($C_{28}H_{31}ClN_2O_3$). The cleaning elements used are ethyl alcohol (CH_3CH_2OH) and diluted nitric acid (HNO_3).

2.2 Synthesis method of MoS_2 nanoflowers

MoS_2 NFs were synthesized using the facial hydrothermal route. In a typical synthetization, 1.76 g of $(NH_4)_6Mo_7O_{24}\cdot 4H_2O$ and 1.52 g of CH_4N_2S were dissolved in 35 mL of ultrapure deionized water, and then the aqueous solution was kept stirring for 1 hour using a magnetic stirrer. Then, the solution is transferred to a 50-mL Teflon-lined hydrothermal reactor (autoclave) that is heated at 200 °C for 24 hours. After that, the autoclave cooled to ambient temperature, and the resulting black powder was washed a few times with CH_3CH_2OH and distilled water. Finally, the sample was dried at 80 °C for 48 hours.

2.3 Photodegradation activity measurements

The photocatalytic activities of the as-synthesized MoS_2 nanoparticles were carried out by monitoring the degradation of MB and RhB dyes under UV (8-watt with 365 nm wavelength) and visible light (150-watt halogen lamp) irradiation. The experiments took place in a 250-mL beaker at ambient temperature. In each experiment, 10 mg of the prepared MoS_2 photocatalyst powder was dispersed in 100 mL of MB or RhB aqueous solution, where the concentration was maintained at 10^{-5} M for both dyes. The suspension was stirred for 30 minutes in the dark in order to achieve the adsorption-desorption equilibrium between the catalyst and the used dye. Then, the solution was maintained under the selected light source (UV or visible light) while the mixture was stirred continuously. The experiments were conducted over a 180-minute period for the sample under UV and over a 60-minute period for the sample under visible light, where 3 mL of the mixture were collected at regular intervals in each case, centrifuged, and examined using a UV-vis spectrometer ranging from 400 to 750 nm.

2.4 Sample characterization

The XRD pattern of the prepared sample was detected using a Philips X-ray diffractometer of the 1710 PW model, which is dependent on CuK_α radiation (wavelength =1.54184 Å) and operates at an applied voltage of 40000 V. Angles ranging from 5° to 80° were measured with a constant angle-scanning speed of 0.06° min^{-1}. FT-IR transmittance spectra were conducted with a NICOLET FT-IR 6700 spectrometer across the range of 400-4000 cm^{-1} for pellets samples mixed with KBr. To explore the morphological characteristics of the produced specimen, FE-SEM images were acquired using a ZIESS Sigma 500 VP scanning electron microscope. Optical absorbance and catalytic data were recorded for the suspension NFs using a Thermo Evolution 300 UV-visible spectrophotometer within a range of 300 to 800 nm. Estimation of the optical energy bandgap was carried out using the Tauc plot based on the UV-visible data. The elemental composition of the synthesized sample was determined using an EDX unit

connected to a scanning electron microscope model, ULTRADRY QUANTA FEG 250 (Field Emission Gun).

3. RESULTS AND DISCUSSION

3.1 X-ray diffraction

The phase and crystalline nature of the as-prepared sample without any heat treatment were analyzed using powder X-ray diffractometer. As shown in Figure 1, the pattern reveals reflections located at 2θ = 13.9º, 29º, 32.6º, 39.46º, 49.78º, and 58.34º that were confirmed as (002), (004), (100), (103), (105), and (110) planes, respectively. As indexed in JCPDS file no. 37-1492, these diffraction peaks in the XRD pattern are highly matched with those of the hexagonal structure of pure MoS_2 (2H-MoS_2) with space group *p6₃/mmc* and a trigonal prismatic coordination between Mo and S atoms [55-57]. No additional peaks were noticed in the XRD pattern, which depicts the high purity of the synthesized specimen. Additionally, the diffraction peaks' broadening suggests the existence of smaller nanodomains [58]. The intense peak (002) that is the main peak of pristine MoS_2, corresponding to 13.9º, indicates that the S-Mo-S layers are well stacked along the C axis [59].

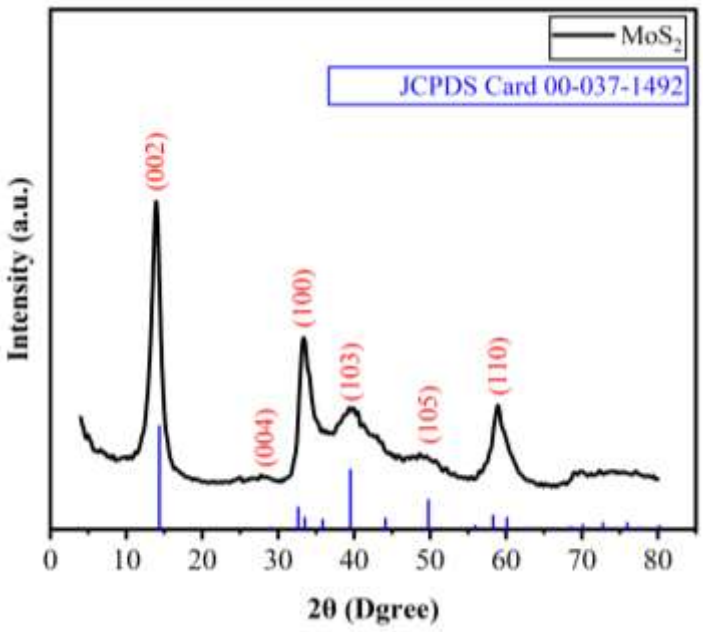

Figure 1. XRD pattern of the as-synthesized MoS_2 nanoflowers.

To gain a deeper understanding of the lattice parameters of MoS_2, the Williamson-Hall (W-H) model displayed in Equation 1 was employed to determine the average grain size (D) and the microstrain (ε) of the nanocrystals [60]. According to W-H, the diffraction line broadening is because of the crystallite size and strain contribution of the MoS_2 NFs (Equation 2), as the strain-induced broadening in MoS_2 NFs results from

crystal imperfections and distortions. The peak broadening of the XRD reflections of the prepared sample includes the instrumental broadening and the particle size broadening, which can be expressed by Equation 3 [60].

$$\beta_{hkl} \cos\theta = \frac{k_s \lambda}{D} + 4\varepsilon \sin\theta \quad (1)$$

$$\beta_{hkl} = \beta_{size} + \beta_{strain} \quad (2)$$

$$\beta^2_{size} = \beta^2_{measured} - \beta^2_{instrumental} \quad (3)$$

Where β is the full-width at half maximum of the diffracted peak measured in radians, k_s is the shape factor assigned to be 0.94, λ is the wavelength of CuK_α radiation, and θ is Bragg's angle in radians.

The strain in the aforementioned equation is known as a uniform deformation model (UDM), as it is thought to be uniform in all crystallographic directions. This model assumes that the crystal is naturally isotropic and that its characteristics are independent on the size of the crystallite (D). By plotting the values of β_{hkl} cos(θ) on the Y-axis as a function of 4sin(θ) on the X-axis and using linear fitting, the Y-intercept was used to estimate D, and the slope of the linear fit was used to determine ε, as shown in Figure 2 [61]. The expansion of the lattice, which causes intrinsic strain in the MoS_2 NFs, is indicated by the positive slope of the carve. This intrinsic strain determined from the slope is very low (0.0٠٧), which gives another confirmation of the smaller strain in the synthesized MoS_2.

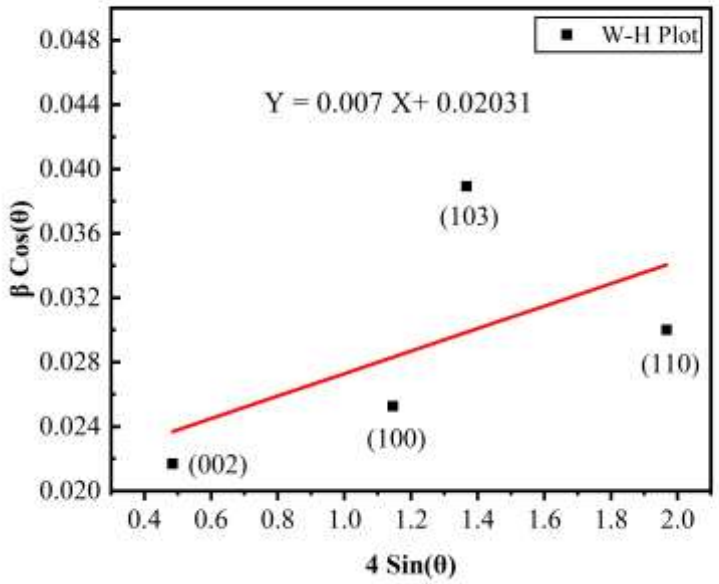

Figure 2. W-H plot of MoS_2 nanoflowers.

The lattice volume (V) of the MoS_2 hexagonal crystal structure and the lattice parameters (a and c) can be calculated via Equation 4 through CellRef software [62]. Equations (5) and (6) can be used to calculate both dislocation density (δ) and theoretical density (ρ), respectively [63]. All the XRD-obtained parameters are declared in Table 1.

$$V = \frac{\sqrt{3}}{2} a^2 c \quad (4)$$

$$\delta = \frac{1}{D^2} \quad (5)$$

$$\rho = \frac{ZM}{N_a V} \quad (6)$$

Where Z represents the number of molecules per unit cell (Z = 2 for MoS_2), M represents the molecular weight, and N_a represents Avogadro's number.

Table 1. XRD structural parameters of MoS_2 nanoparticles: calculated values of lattice constants (a) and (c), unit cell volume (V), average grain size (D), lattice strain (ε), theoretical density (ρ), and dislocation density (δ).

Sample	a (Å)	c (Å)	V (Å^3)	D_{XRD} (nm)	ρ (gm/cm^3)	ε	δ (nm)$^{-2}$
MoS_2	3.14	12.36	105.31	6.84	4.86	0.007	0.0214

3.2 Scanning electron microscopy

The surface morphology of the as-synthesized MoS_2 photocatalyst was investigated at different magnifications using the FE-SEM technique. As shown in Figure 3a, a typical low-magnification (3 k x) recorded image shows that pristine MoS_2 exhibits a flower-like architecture that is assembled from MoS_2 nanosheets. A higher-magnification (40 k x) image is recorded, as shown in Figure 3b, which confirms that each flower-like structure is composed of thin sheets that are slightly curved. The observed average width of the MoS_2 nanosheets is about several hundred nanometers.

Vattikuti et al. [64] reported in their previous work that the MoS_2 sample synthesized by using thiourea as a source of sulfur has multilayer nanosheets of a few nanometers in size. The use of precursor materials, specifically ammonium molybdate and thiourea, is crucial in determining the shape of the MoS_2 through this reaction. In the hydrothermal process, ammonium molybdate produces MoO_4^- and ammonium ions, while thiourea serves as the source of sulfur. As MoO_4^- ions react with sulfur ions, MoS_2 is formed. The presence of remaining ammonia minimizes the stacking of MoS_2 nanostructures, resulting in a spherical, flower-like morphology through self-assembly [65]. This particular morphology is frequently observed for MoS_2 [66]. Ghaleghafi et al. [67] were able to synthesize MoS_2 in the form of flower-like microspheres composed of 2D nanosheets using the simple hydrothermal method, with a nanosheet thickness of about 8-62 nm.

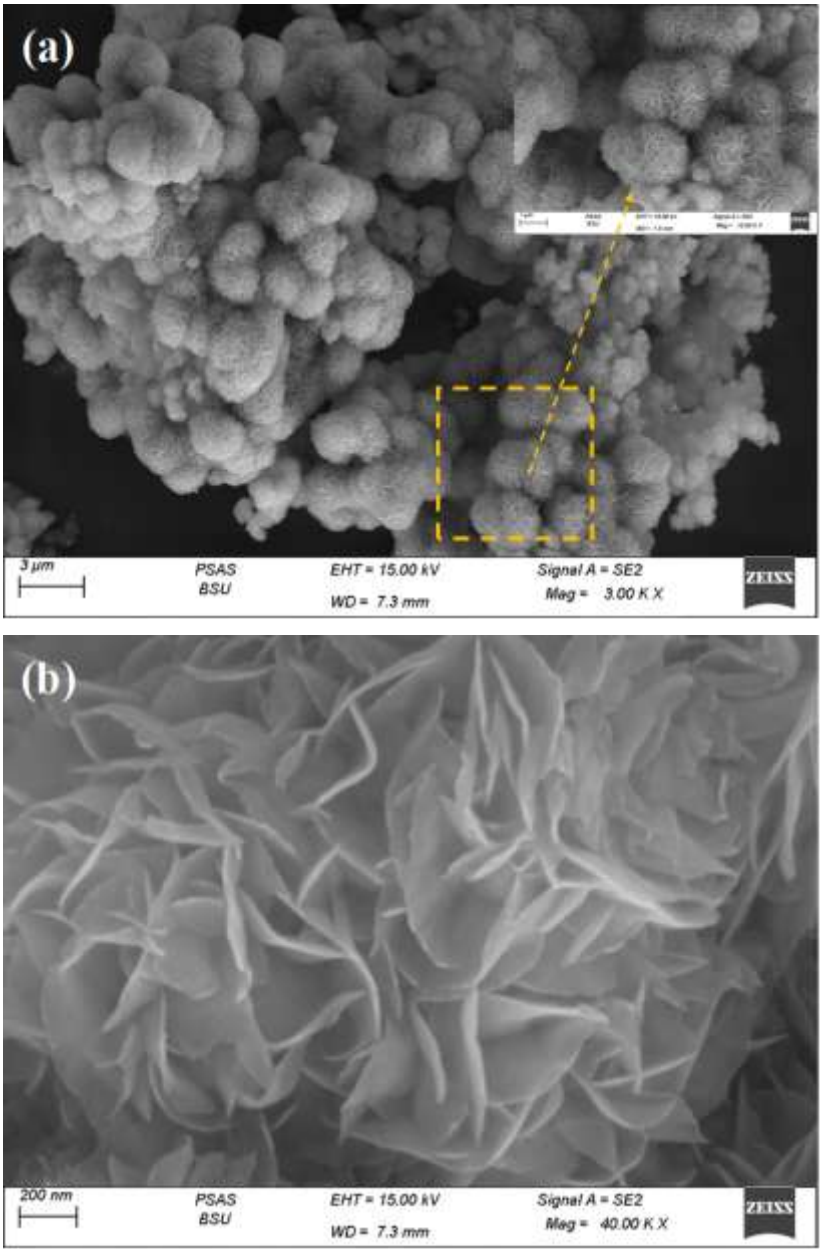

Figure 3. FE-SEM images of pure MoS_2 nanoparticles at the magnification of (a) 3 k x, (b) 40 k x.

3.3 Fourier Transform Infra‑Red Spectroscopy

FT-IR spectroscopy, which is a non-destructive technique, was employed to acquire information about the bending and stretching vibrations of the functional groups found in the as-prepared MoS_2 NFs. Figure 4 describes the FT-IR spectra of the sample being examined, where there are eight absorption bands at 490 cm^{-1}, 570 cm^{-1}, 613 cm^{-1}, 915 cm^{-1}, 1090 cm^{-1}, 1400 cm^{-1}, 1630 cm^{-1}, and 3445 cm^{-1}. The absorption characteristic bands at 490 cm^{-1}, 570 cm^{-1}, and 613 cm^{-1} are due to the Mo-S bond stretching vibrations, and the characteristic weak band shown at 915 cm^{-1} is attributed to the S-S stretching bond [68-70]. The stretching vibrations of the hydroxyl-group and Mo-O vibrations are

accountable for the absorption bands located at 1090 cm^{-1}, 1400 cm^{-1}, and 1630 cm^{-1}, while the broad band centered around 3445 cm^{-1} is caused by the symmetrical stretching vibration of hydroxyls (O-H) [69-72].

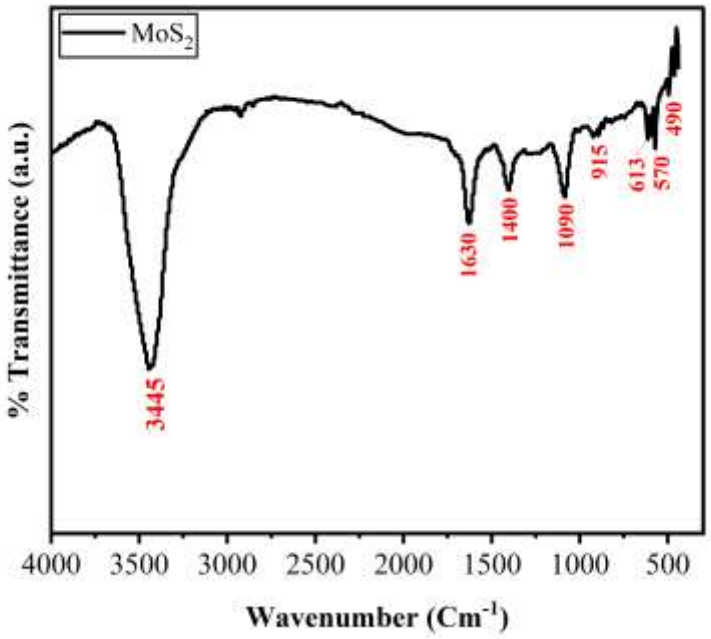

Figure 4. FT-IR spectra of the as-prepared MoS_2 nanoflowers.

3.4 Energy Dispersive X-Ray Spectroscopy

The high spatial resolution EDX spectra of the as-synthesized MoS_2, depicted in Figure 5, provide clear evidence of the existence of Mo and S atoms as expected. These peaks show that there are no foreign impurities. Based on the EDX spectra, the peaks of Mo are observed at 2.47 keV, indicating L_α and L_β characteristic lines, while sulfur exhibits its peak at 2.48 keV, representing the K_α characteristic line. These peaks overlap due to the close proximity of the energy levels of S and Mo [63, 73]. Also, as shown in the inset table of Figure 5, the EDX quantitative analysis depicts that the composition of Mo and S in the MoS_2 NFs is determined to be close to 1:2, which is very close to the theoretical value [74]. A tiny quantity of oxygen (K_α, 0.523 keV), if it exists at all, is indicated in the elemental map displayed in the detected spectra [75].

3.5 Ultraviolet Visible Spectroscopy

UV-visible absorption spectroscopy is an essential method of measurement that is necessary for characterizing the electronic band structures of different materials. The optical properties of pristine MoS_2 NFs suspended in distilled water have been analyzed using UV-vis absorption spectroscopy in the range of 300-800 nm. Figure 6a provides a visual representation of the absorbance spectra of the as-prepared MoS_2. It can be observed that there are three distinct bands. The first band, located within the wavelength

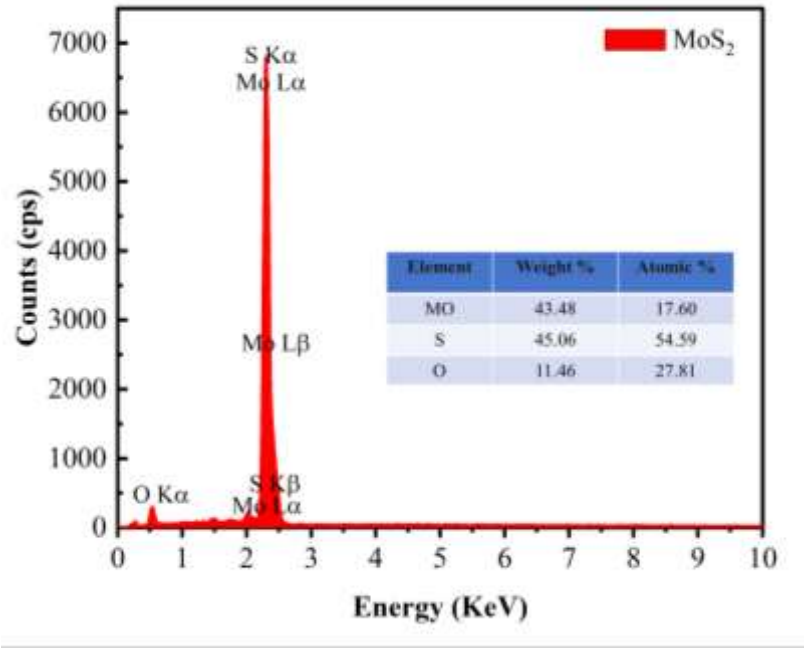

Figure 5. EDX spectra of MoS_2 nanoflowers.

range of 450-480 nm, is owing to the electronic transition from the valance band (VB) (occupied d_z^2 orbital) to the conduction band (CB) (unoccupied $d_{xy-x}{}^2{}_{-y}{}^2$ or d_{xz-yz} orbitals). This transition is assigned as C exciton, while the additional two absorption bands, seen at approximately 630 nm and 680 nm, occur due to the excitonic transitions of the first and second Brillouin zones at the K/K' points [67, 69, 76-78]. These two distinct optical transitions are assigned as A and B excitons [67]. This suggests that MoS_2 nanoflowers exhibit a narrow optical band gap as a result of the quantum confinement effect [79]. Equation 7 can be utilized to compute the absorption coefficient α [80].

$$\alpha = \frac{2.303\,\rho \times 10^3}{\mathrm{Lcm}}\mathrm{A} \tag{7}$$

Where the symbols ρ and A represent the theoretical density and the absorbance of the sample, respectively, while L, c, and m represent the distance light passing through the solution (assumed to be 1 cm), the molar mass, and the molar concentration, respectively.

The E_g of the MoS_2 photocatalyst can be determined through the utilization of the Tauc formula [81]:

$$(\alpha h\nu)^n = B\left(h\nu - E_g\right) \tag{8}$$

Where α represents the absorption coefficient measured in cm^{-1}, h is Planck's constant measured in Joule second, ν is the photon's frequency measured in Hz, B is a constant that does not depend on the energy of the photons, and n is a constant with four possible values: 2, 1/2, 3, or 1/3. These four values correspond to direct allowed transitions,

indirect allowed transitions, direct forbidden transitions, and indirect forbidden transitions, respectively. The value of E_g can be determined by extending the linear portion of the graph where $(\alpha h\nu)^2$ is plotted on the Y-axis against the photon energy ($h\nu$) on the X-axis to the X-axis itself (Figure 6b). For pure MoS_2 , E_g is calculated to be 1.82 eV, showing strong consistency with earlier studies [82-85]. This calculated bandgap makes the produced MoS_2 NFs very responsive to visible light and can be utilized as photocatalysts in the visible light region.

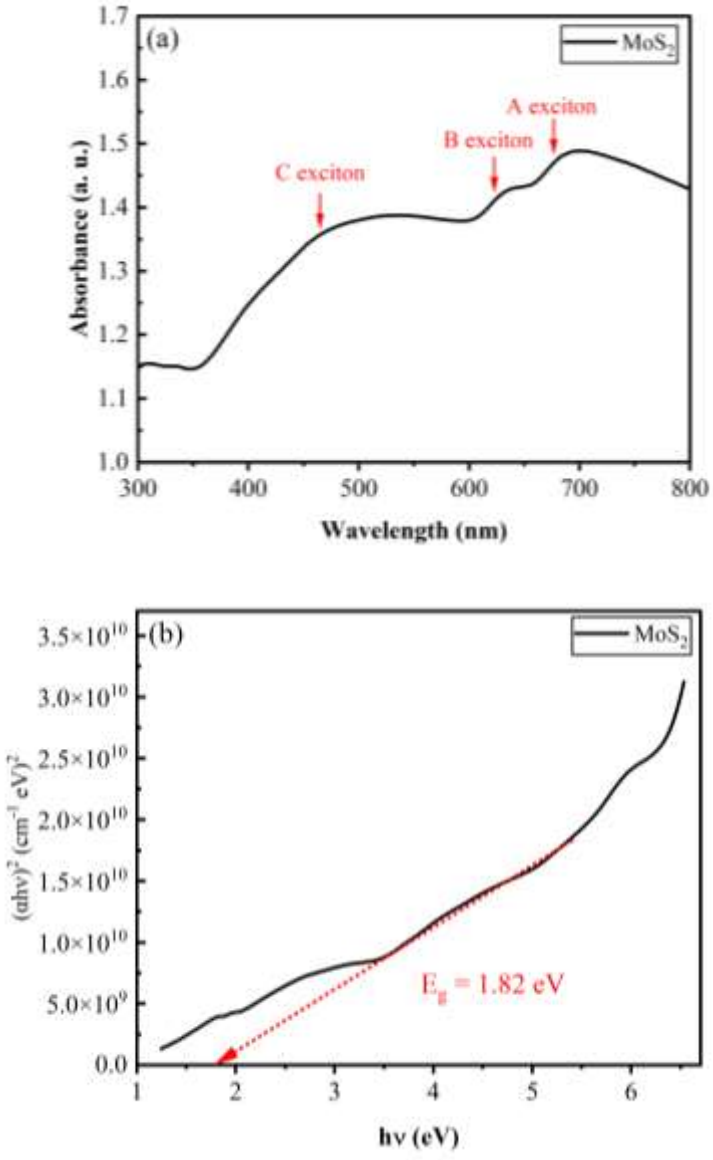

Figure 6. (a) UV- vis absorbance spectra of MoS_2 nanoparticles, (b) Tauc's plot for direct optical bandgap of pristine MoS_2 nanoparticles.

3.6 Photocatalytic study

3.6.1 Photocatalytic activity evaluation

To confirm its potential for ecological application in the removal of contaminants from wastewater, the degradation activity of the as-prepared MoS_2 NFs was assessed using MB and RhB dyes under UV and visible-light irradiation. The degradation process was observed by tracking the variance in the absorption intensity of the main peak of each dye as a function of the exposure time. The main absorption peak of RhB dye exists around 554 nm, while the main absorption peak exists around 664 nm for MB dye [86-88]. As shown in Figure 7a, MB and RhB are very hard to degrade in the absence of the MoS_2 photocatalyst, which proves that the photolysis of MB and RhB can be neglected. Figures 7b-e display the time-dependent UV-visible absorption spectra of MB and RhB solutions in the presence of MoS_2 NFs under UV irradiation up to 180 minutes and visible light up to 60 minutes. The photocatalytic degradation increases with increasing irradiation time, and the dye's degradation percentage is represented by Equation (9) [69, 73]:

$$\text{Degradation Efficiency (\%)} = \frac{C_0 - C_t}{C_0} \times 100 \tag{9}$$

Where C_0 and C_t represent the absorption values detected by the UV-visible spectrophotometer at 0 and t minutes, respectively. It is noted from the calculated degradation efficiency values as shown in Figure 8 that MoS_2 NFs are more efficient to degrade RhB than MB under UV illumination, where the efficiency was 84.31% in the case of RhB dye while it was 75.97% in the case of MB dye through 180 minutes However, when using visible light as a source of illumination, an opposite behavior was detected, and MoS_2 was more efficient to degrade MB (84.25%) than RhB (73.99%) through 60 minutes of irradiation. These results give a very strong empirical evidence that MoS_2 as a photocatalyst can have different efficiencies in removing specific types of pollutants depending upon the wavelength of the light source utilized, keeping all the other experimental factors constant.

Relative degradation is presented by the C_t/C_0 ratio, as shown in Figure 9, when using UV and visible light as sources of irradiation, respectively. It is clear from Figure 9a that, in the case of using the UV lamp, the photocatalytic degradation speed of the MB dye is very close to that of the RhB dye, while the RhB dye is still faster, especially in the first 20 minutes of the irradiation period. Moreover, in the case of visible light, the MB dye degraded faster than that of RhB, as shown in Figure 9b. In addition, the Langmiur-Henshelwood (L-H) model [89], which is considered a pseudo first-order kinetic mode, is used to determine the recombination rate constant (γ) of the MB and RhB dyes using the given Equation [89].

$$\ln\left(\frac{C_0}{C_t}\right) = \gamma t \tag{10}$$

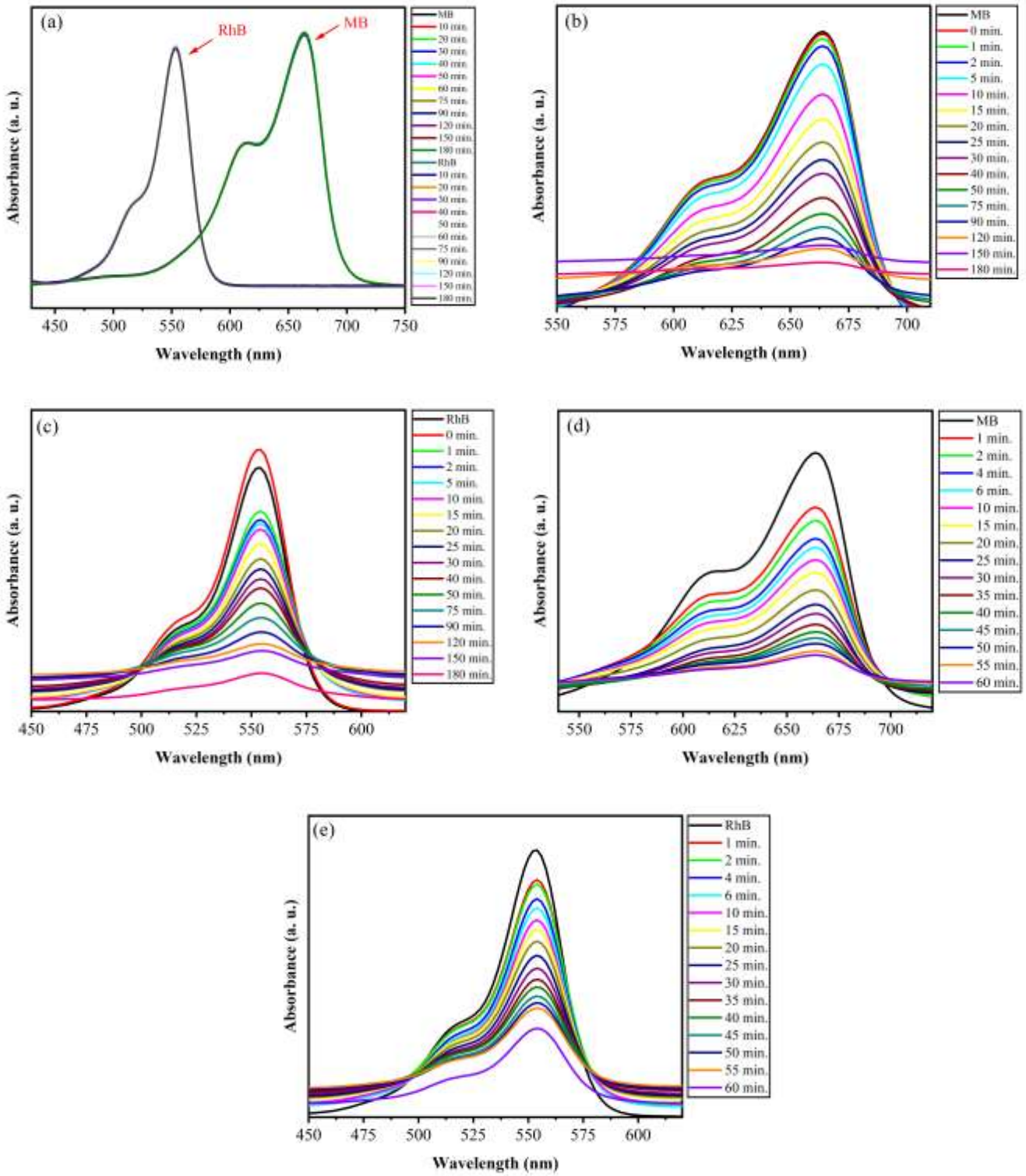

Figure 7. Time-dependent UV-visible absorption spectra of (a) only MB or RhB without photocatalyst under UV-light, (b) MB in the presence of MoS_2 under UV-light, (c) RhB in the presence of MoS_2 under UV-light, (d) MB in the presence of MoS_2 under visible-light, and (e) RhB in the presence of MoS_2 under visible-light.

The relation between $\ln(C_0/C_t)$ and the duration of irradiation exposure reveals the oxidation process of MB and RhB dyes by the MoS_2 NFs [90]. This relation exhibits a suitable pseudo-first-order kinetic model. Upon calculation, the rate constant, in min^{-1}, for the dye solution under UV and visible light was determined and shown in Figures 10a and 10b. As indicated by the kinetic analysis, a minimal kinetic rate constant is estimated for MB and RhB dyes in the absence of MoS_2 photocatalyst. While the use of pure MoS_2 increases the kinetic constant more than nine times in the case of MB under visible light irradiation. This exceptional photocatalytic activity of the MoS_2 NFs when exposed to visible light was probably because of the narrow bandgap (1.82 eV), which absorbs light across the entire visible range of wavelengths, and the more defective sites, such as edge sites [71].

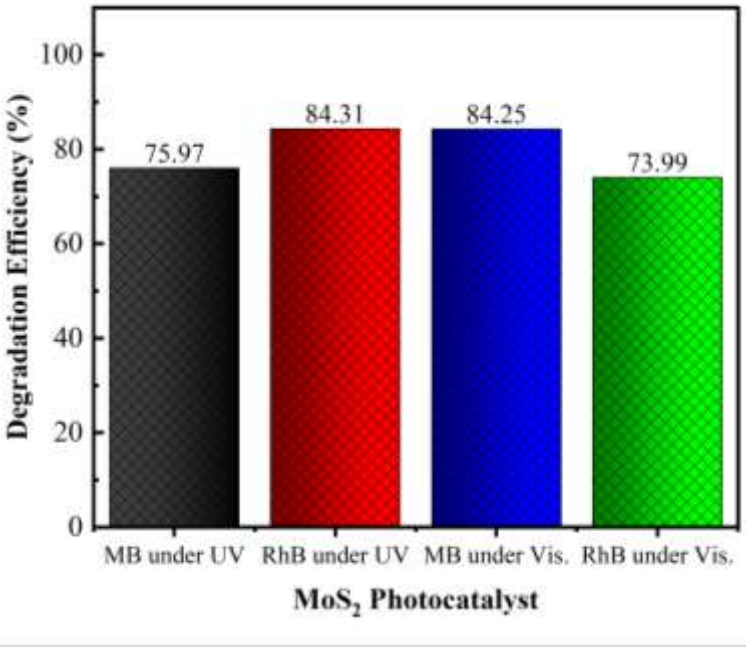

Figure 8. Photocatalytic degradation efficiency of MB and RhB using MoS_2 nanostructure under UV for 180 minutes and visible light irradiation for 60 minutes.

3.6.2 Photocatalytic mechanism

The UV and visible light photocatalytic degradation activity of MB and RhB in the presence of MoS_2 NFs can be most effectively explained by the mechanism of the process, as shown in Figure 11. Firstly, due to the narrow energy bandgap of the MoS_2 NFs, both electrons (e^-) and holes (h^+) are produced. Electrons in the CB interact with the available oxygen to form superoxide radicals ($^{\bullet}O_2^-$), which react with H^+ ions to form H_2O_2, and finally H_2O_2 decomposes into hydroxyl radicals ($^{\bullet}OH$) [90]. In the same manner, $^{\bullet}OH$ radicals are created when holes in the VB react with water. Consequently, the $^{\bullet}OH$ radicals produced effectively degrade the absorbed dyes at normal room temperature through a straightforward process of magnetic stirring. The generation of radicals, degradation of dyes, and production of products occur in the reactions represented in Equations 11 to 17 [69, 71].

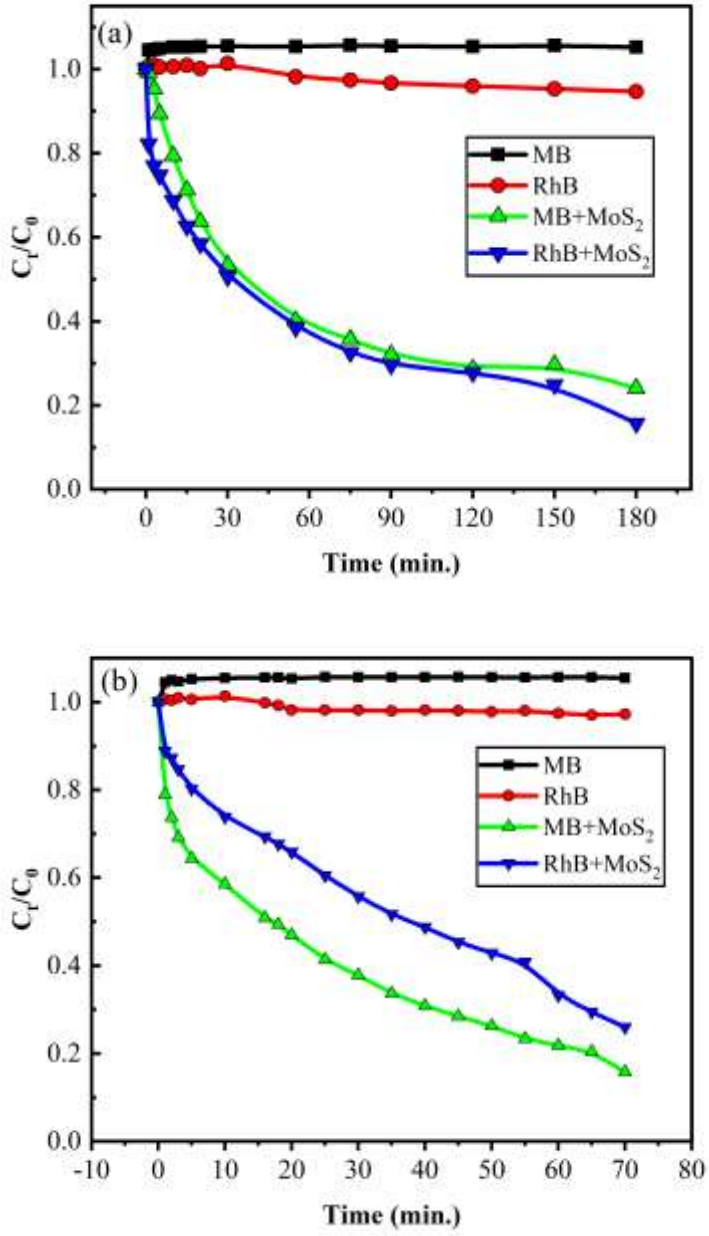

Figure 9. Photocatalytic activity representation through the change in the C_t/C_0 ratio versus the light irradiation time of MoS_2 nanoflowers against MB and RhB dyes under (a) UV light for 180 minutes and (b) visible light for 60 minutes.

$$MoS_2\ NFs + UV\ or\ Visible\ light \rightarrow MoS_2\ NFs(e^- + h^+) \quad (11)$$

$$e^- + O_2 \longrightarrow {}^{\bullet}O_2^- \quad (12)$$

$$H_2O \longrightarrow H^+ + OH^- \quad (13)$$

$$^{\bullet}O_2^- + H^+ \longrightarrow H_2O_2 \quad (14)$$

$$H_2O_2 + e^- \longrightarrow {}^{\bullet}OH + OH^- \quad (15)$$

$$h^+ + OH^- \longrightarrow {}^{\bullet}OH \quad (16)$$

$$^{\bullet}OH + \text{MB or RhB Dye} \longrightarrow CO_2 + H_2O \text{ (degradation products)} \quad (17)$$

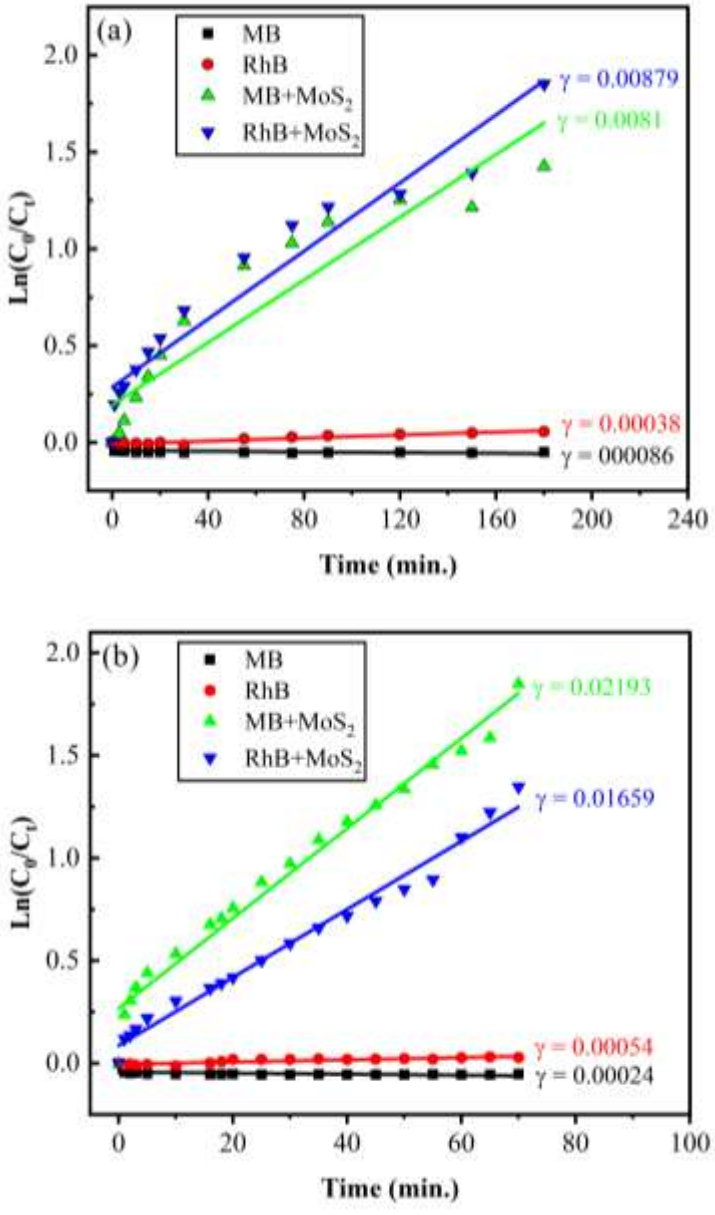

Figure 10. The pseudo first order kinetics fitted data for MB and RhB photodegradation by MoS_2 under the illumination of (a) UV light for 180 minutes and (b) visible light for 60 minutes.

In general, these pairs of electrons and holes tend to recombine together again, and only a small number of charges are moved to the reaction sites in order to convert H^+ to H_2 during the process of photocatalysis. Therefore, it is necessary to prevent the recombination of the charge pairs generated by light in order to increase the efficiency of photocatalysis [91]. The position of the energy bandgap (CB and VB) in MoS_2 was determined by utilizing the subsequent mathematical formulas [92, 93]:

$$E_{CB} = X - E^e - 0.5E_g \quad (18)$$

$$E_{CB} = E_{VB} - E_g \quad (19)$$

where E_{CB} and E_{VB} represent the CB and VB edge potentials, respectively, X represents the electronegativity of the semiconductor, which is equal to 5.32 eV in the case of MoS_2, E^e is the energy of unbound electrons on the hydrogen scale (4.50 eV), and E_g is the energy bandgap of the semiconductor (1.85 eV for MoS_2) as calculated from diffuse reflectance spectroscopy (DRS) data. By using the above-mentioned equation, the E_{CB} obtained for MoS_2 was determined to be -0.11 eV [91, 93].

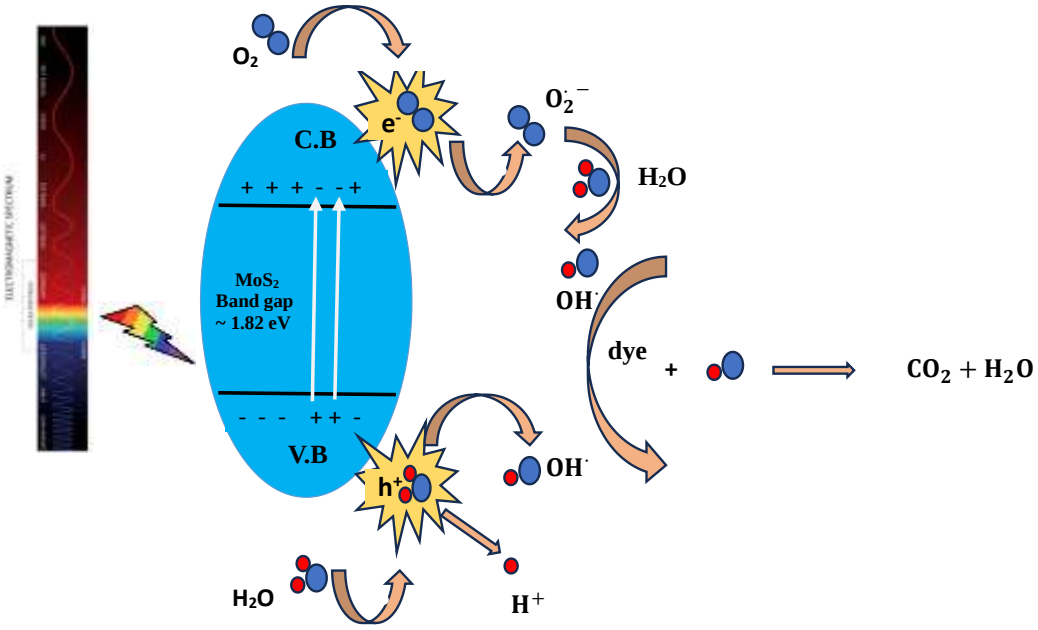

Figure 11. Schematic representation for the dye degradation mechanism using MoS_2 nanostructure photocatalyst.

3.6.3 Reusability of MoS_2 Photocatalyst

The stability of MoS_2 NFs photocatalyst for the photodegradation of MB under UV light irradiation was examined. Figure 12 displays the reusability of the MoS_2 NFs over three consecutive cycles using identical experimental conditions. It is evident from

the graph that there was only a minimal decrease (from 73.50% in the 1st cycle to 71.36% in the 3rd cycle) in the effectiveness of photocatalytic activity for MB removal. The slight decline in photocatalytic activity may be attributed to the loss of catalyst during the recovery process, which includes centrifugation, washing, and subsequent drying.

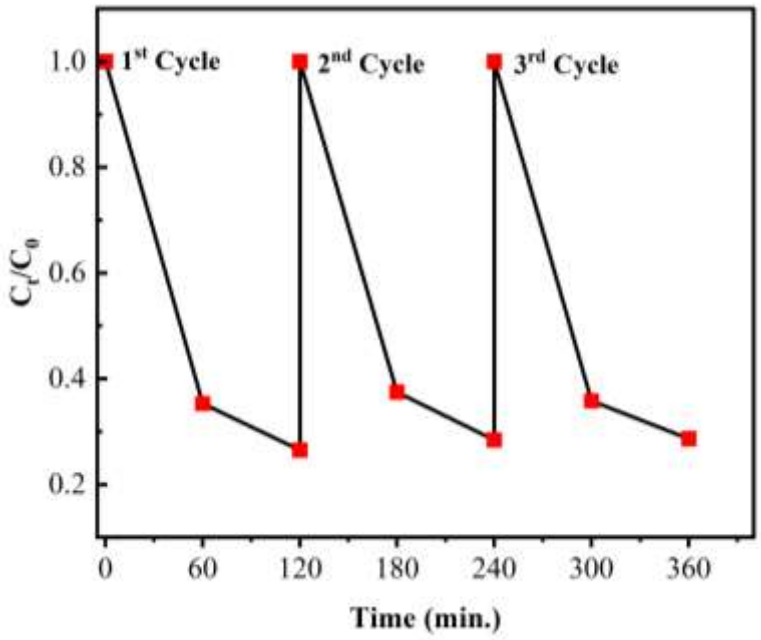

Figure 12. Recyclability in the presence of MoS_2 nanostructure for photocatalytic degradation of MB dye under UV irradiation.

4. CONCLUSION

In summary, MoS_2 photocatalyst was successfully synthesized via the facile hydrothermal method. The XRD analysis reveals the formation of a pure semiconducting 2H-MoS_2 phase with a space group of $p6_3/mmc$. The W-H model was employed to calculate the average grain size and the lattice strain, which were found to be 6.84 nm and 0.007, respectively. The FE-SEM images clearly confirmed the formation of MoS_2 NFs composed of thin nanosheets that are slightly curved, which provide more essential active sites for the photocatalytic reactions. The appearance of the absorption characteristic bands between 490 cm^{-1} and 615 cm^{-1} owing to the Mo-S bond and at 915 cm^{-1} due to the S-S bond through FT-IR analysis also confirmed the formation of the MoS_2 nanostructure. The detection of Mo and S elements using EDX analysis confirmed the proposed formation of pure MoS_2 nanocrystals. The as-prepared MoS_2 was utilized as a potential photocatalyst for the degradation of MB and RhB under the irradiation of UV and visible light in a comparative way. The results showed that the photocatalytic degradation of RhB dye was faster and more efficient, with a kinetic rate constant and efficiency of 0.00879 min^{-1} and 84.31%, respectively, than the degradation of MB under

UV irradiation. However, the photodegradation of MB was faster and more efficient, with a kinetic rate constant and efficiency of 0.0219 min^{-1} and 84.25, respectively, than that of RhB under visible light illumination. The degradation of these two dyes under the irradiation sources was attributed to the characteristics of the MoS_2 NFs, namely the narrow E_g (1.82 eV) as estimated via Tauc's plot through UV-vis spectroscopy and the relatively large number of active edge sites. Furthermore, the photocatalytic mechanism has been discussed in detail, and it is reported that just the $^{\bullet}OH$ radicals are produced by the MoS_2 NFs, which are the main factors responsible for the MB and RhB degradation. Finally, MoS_2 NFs have shown excellent stability when used in degrading MB dye under UV light over three complete cycles, where the experiment reflected a minimal decrease from 73.50% in the first cycle to 71.36% in the last cycle.

REFERENCES

[1] Ritika, M. Kaur, A. Umar, S. K. Mehta, S. Singh, S. K. Kansal, H. Fouad, and O. Y. Alothman, "Rapid solar-light driven superior photocatalytic degradation of methylene blue using MoS_2-ZnO heterostructure nanorods photocatalyst," Materials, vol. 11, p. 2254, 2018.

[2] W. Guan and S. Tian, "The modified chitosan for dyeing wastewater treatment via adsorption and flocculation," Science of Advanced Materials, vol. 9, pp. 1603-1609, 2017.

[3] M. Namdeo, "Magnetite nanoparticles as effective adsorbent for water purification-a review," Advances in Recycling & Waste Management, vol. 2, pp. 126-129, 2018.

[4] A. Kaur, A. Umar, W. A. Anderson, and S. K. Kansal, "Facile synthesis of CdS/TiO_2 nanocomposite and their catalytic activity for ofloxacin degradation under visible illumination," Journal of Photochemistry and Photobiology A: Chemistry, vol. 360, pp. 34-43, 2018.

[5] P. Sharma and M. S. Mehata, "Rapid sensing of lead metal ions in an aqueous medium by MoS_2 quantum dots fluorescence turn-off," Materials Research Bulletin, vol. 131, p. 110978, 2020.

[6] V. Sharma and M. S. Mehata, "Synthesis of photoactivated highly fluorescent Mn^{2+}-doped ZnSe quantum dots as effective lead sensor in drinking water," Materials Research Bulletin, vol. 134, p. 111121, 2021.

[7] P. Sharma and M. S. Mehata, "Colloidal MoS_2 quantum dots based optical sensor for detection of 2, 4, 6-TNP explosive in an aqueous medium," Optical Materials, vol. 100, p. 109646, 2020.

[8] S. Dervin, D. D. Dionysiou, and S. C. Pillai, "2D nanostructures for water purification: graphene and beyond," Nanoscale, vol. 8, pp. 15115-15131, 2016.

[9] M. Junaid, M. Imran, M. Ikram, M. Naz, M. Aqeel, H. Afzal, H. Majeed, and S. Ali, "The study of Fe-doped CdS nanoparticle-assisted photocatalytic degradation of organic dye in wastewater," Applied Nanoscience, vol. 9, pp. 1593-1602, 2019.

[10] K. R. Kunduru, M. Nazarkovsky, S. Farah, R. P. Pawar, A. Basu, and A. J. Domb, "Nanotechnology for water purification: applications of nanotechnology methods in wastewater treatment," Water purification, pp. 33-74, 2017.

[11] F. Han, V. S. R. Kambala, M. Srinivasan, D. Rajarathnam, and R. Naidu, "Tailored titanium dioxide photocatalysts for the degradation of organic dyes in wastewater treatment: a review," Applied Catalysis A: General, vol. 359, pp. 25-40, 2009.

[12] M. N. Chong, B. Jin, C. W. Chow, and C. Saint, "Recent developments in photocatalytic water treatment technology: a review," Water research, vol. 44, pp. 2997-3027, 2010.

[13] X. Liu, A. Jin, Y. Jia, T. Xia, C. Deng, M. Zhu, C. Chen, and X. Chen, "Synergy of adsorption and visible-light photocatalytic degradation of methylene blue by a bifunctional Z-scheme heterojunction of WO_3/g-C_3N_4," Applied Surface Science, vol. 405, pp. 359-371, 2017.

[14] S. Vadivel, D. Maruthamani, A. Habibi-Yangjeh, B. Paul, S. S. Dhar, and K. Selvam, "Facile synthesis of novel $CaFe_2O_4$/g-C_3N_4 nanocomposites for degradation of methylene blue under visible-light irradiation," Journal of colloid and interface science, vol. 480, pp. 126-136, 2016.

[15] M. K. Singh and M. S. Mehata, "Enhanced photoinduced catalytic activity of transition metal ions incorporated TiO_2 nanoparticles for degradation of organic dye: absorption and photoluminescence spectroscopy," Optical Materials, vol. 109, p. 110309, 2020.

[16] M. K. Singh and M. S. Mehata, "Phase-dependent optical and photocatalytic performance of synthesized titanium dioxide (TiO_2) nanoparticles," Optik, vol. 193, p. 163011, 2019.

[17] S. Bishnoi, B. Rajesh, G. Swati, V. V. Jaiswal, M. Sahu, P. Singh, and D. Haranath, "Structural, morphological, photoluminescence and electrical characterization of aluminium doped ZnO phosphors for solar cell applications," Materials Today: Proceedings, vol. 5, pp. 610-619, 2018.

[18] M. Velický and P. S. Toth, "From two-dimensional materials to their heterostructures: An electrochemist's perspective," Applied Materials Today, vol. 8, pp. 68-103, 2017.

[19] H. Wang, H. Yuan, S. S. Hong, Y. Li, and Y. Cui, "Physical and chemical tuning of two-dimensional transition metal dichalcogenides," Chemical Society Reviews, vol. 44, pp. 2664-2680, 2015.

[20] D. Kaplan, Y. Gong, K. Mills, V. Swaminathan, P. Ajayan, S. Shirodkar, and E. Kaxiras, "Excitation intensity dependence of photoluminescence from monolayers of MoS_2 and WS_2/MoS_2 heterostructures," 2D Materials, vol. 3, p. 015005, 2016.

[21] L. Chen, Y. Feng, X. Zhou, Q. Zhang, W. Nie, W. Wang, Y. Zhang, and C. He, "One-pot synthesis of MoS_2 nanoflakes with desirable degradability for photothermal cancer therapy," ACS applied materials & interfaces, vol. 9, pp. 17347-17358, 2017.

[22] B. L. Li, M. I. Setyawati, L. Chen, J. Xie, K. Ariga, C.-T. Lim, S. Garaj, and D. T. Leong, "Directing assembly and disassembly of 2D MoS_2 nanosheets with DNA for drug delivery," ACS applied materials & interfaces, vol. 9, pp. 15286-15296, 2017.

[23] X. Zong, H. Yan, G. Wu, G. Ma, F. Wen, L. Wang, and C. Li, "Enhancement of photocatalytic H_2 evolution on CdS by loading MoS_2 as cocatalyst under visible light irradiation," Journal of the American Chemical Society, vol. 130, pp. 7176-7177, 2008.

[24] J. Kibsgaard, Z. Chen, B. N. Reinecke, and T. F. Jaramillo, "Engineering the surface structure of MoS_2 to preferentially expose active edge sites for electrocatalysis," Nature materials, vol. 11, pp. 963-969, 2012.

[25] D. Voiry, M. Salehi, R. Silva, T. Fujita, M. Chen, T. Asefa, V. B. Shenoy, G. Eda, and M. Chhowalla, "Conducting MoS_2 nanosheets as catalysts for hydrogen evolution reaction," Nano letters, vol. 13, pp. 6222-6227, 2013.

[26] J. Yu, X. Ma, W. Yin, and Z. Gu, "Synthesis of PVP-functionalized ultra-small MoS_2 nanoparticles with intrinsic peroxidase-like activity for H_2O_2 and glucose detection," RSC advances, vol. 6, pp. 81174-81183, 2016.

[27] X. Yang, J. Li, T. Liang, C. Ma, Y. Zhang, H. Chen, N. Hanagata, H. Su, and M. Xu, "Antibacterial activity of two-dimensional MoS_2 sheets," Nanoscale, vol. 6, pp. 10126-10133, 2014.

[28] C. Ataca and S. Ciraci, "Dissociation of H_2O at the vacancies of single-layer MoS_2," Physical Review B, vol. 85, p. 195410, 2012.

[29] M. Park, Y. J. Park, X. Chen, Y. K. Park, M. S. Kim, and J. H. Ahn, "MoS_2- based tactile sensor for electronic skin applications," Advanced Materials, vol. 28, pp. 2556-2562, 2016.

[30] M. A. Bissett, I. A. Kinloch, and R. A. Dryfe, "Characterization of MoS_2–graphene composites for high-performance coin cell supercapacitors," ACS applied materials & interfaces, vol. 7, pp. 17388-17398, 2015.

[31] Y. Teng, H. Zhao, Z. Zhang, Z. Li, Q. Xia, Y. Zhang, L. Zhao, X. Du, Z. Du, and P. Lv, "MoS_2 nanosheets vertically grown on graphene sheets for lithium-ion battery anodes," ACS nano, vol. 10, pp. 8526-8535, 2016.

[32] L. David, R. Bhandavat, and G. Singh, "MoS_2/graphene composite paper for sodium-ion battery electrodes," ACS nano, vol. 8, pp. 1759-1770, 2014.

[33] Y. Yoon, K. Ganapathi, and S. Salahuddin, "How good can monolayer MoS_2 transistors be?," Nano letters, vol. 11, pp. 3768-3773, 2011.

[34] Y. Chen, X. Wang, P. Wang, H. Huang, G. Wu, B. Tian, Z. Hong, Y. Wang, S. Sun, and H. Shen, "Optoelectronic properties of few-layer MoS_2 FET gated by ferroelectric relaxor polymer," ACS applied materials & interfaces, vol. 8, pp. 32083-32088, 2016.

[35] H. Xie, B. Jiang, B. Liu, Q. Wang, J. Xu, and F. Pan, "An investigation on the tribological performances of the SiO_2/MoS_2 hybrid nanofluids for magnesium alloy-steel contacts," Nanoscale research letters, vol. 11, pp. 1-17, 2016.

[36] L. Ye, D. Wang, and S. Chen, "Fabrication and enhanced photoelectrochemical performance of MoS_2/S-doped g-C_3N_4 heterojunction film," ACS applied materials & interfaces, vol. 8, pp. 5280-5289, 2016.

[37] K. Peng, P. Wan, H. Wang, L. Zuo, M. Niu, L. Su, L. Zhuang, and X. Li, "Unraveling the morphology effect of kandite supporting MoS_2 nanosheets for enhancing electrocatalytic hydrogen evolution," Applied Clay Science, vol. 212, p. 106211, 2021.

[38] K. Peng, J. Zhou, H. Gao, J. Wang, H. Wang, L. Su, and P. Wan, "Emerging 1D/2D Heteronanostructure Integrating SiC Nanowires with MoS_2 Nanosheets for Efficient Electrocatalytic Hydrogen Evolution."

[39] K. Peng, H. Wang, H. Gao, P. Wan, M. Ma, and X. Li, "Emerging hierarchical ternary 2D nanocomposites constructed from montmorillonite, graphene and MoS_2 for enhanced electrochemical hydrogen evolution," Chemical Engineering Journal, vol. 393, p. 124704, 2020.

[40] C. Ataca, H. Sahin, E. Akturk, and S. Ciraci, "Mechanical and electronic properties of MoS_2 nanoribbons and their defects," The Journal of Physical Chemistry C, vol. 115, pp. 3934-3941, 2011.

[41] J. Heising and M. G. Kanatzidis, "Structure of restacked MoS_2 and WS_2 elucidated by electron crystallography," Journal of the American Chemical Society, vol. 121, pp. 638-643, 1999.

[42] C. Lee, H. Yan, L. E. Brus, T. F. Heinz, J. Hone, and S. Ryu, "Anomalous lattice vibrations of single-and few-layer MoS_2," ACS nano, vol. 4, pp. 2695-2700, 2010.

[43] D. Chiappe, E. Scalise, E. Cinquanta, C. Grazianetti, B. van den Broek, M. Fanciulli, M. Houssa, and A. Molle, "Two- dimensional Si nanosheets with local hexagonal structure on a MoS_2 surface," Advanced Materials, vol. 26, pp. 2096-2101, 2014.

[44] A. Splendiani, L. Sun, Y. Zhang, T. Li, J. Kim, C.-Y. Chim, G. Galli, and F. Wang, "Emerging photoluminescence in monolayer MoS_2," Nano letters, vol. 10, pp. 1271-1275, 2010.

[45] K. Wang, J. Wang, J. Fan, M. Lotya, A. O'Neill, D. Fox, Y. Feng, X. Zhang, B. Jiang, and Q. Zhao, "Ultrafast saturable absorption of two-dimensional MoS_2 nanosheets," ACS nano, vol. 7, pp. 9260-9267, 2013.

[46] K. Wang, Y. Feng, C. Chang, J. Zhan, C. Wang, Q. Zhao, J. N. Coleman, L. Zhang, W. J. Blau, and J. Wang, "Broadband ultrafast nonlinear absorption and nonlinear refraction of layered molybdenum dichalcogenide semiconductors," Nanoscale, vol. 6, pp. 10530-10535, 2014.

[47] Y. Li, N. Dong, S. Zhang, X. Zhang, Y. Feng, K. Wang, L. Zhang, and J. Wang, "Giant two- photon absorption in monolayer MoS_2," Laser & Photonics Reviews, vol. 9, pp. 427-434, 2015.

[48] Y.-H. Lee, X.-Q. Zhang, W. Zhang, M.-T. Chang, C.-T. Lin, K.-D. Chang, Y.-C. Yu, J. T.-W. Wang, C.-S. Chang, and L.-J. Li, "Synthesis of large-area MoS_2 atomic layers with chemical vapor deposition," arXiv preprint arXiv:1202.5458, 2012.

[49] Z. Cai, B. Liu, X. Zou, and H.-M. Cheng, "Chemical vapor deposition growth and applications of two-dimensional materials and their heterostructures," Chemical reviews, vol. 118, pp. 6091-6133, 2018.

[50] S. Zhang, N. Dong, N. McEvoy, M. O'Brien, S. Winters, N. C. Berner, C. Yim, Y. Li, X. Zhang, and Z. Chen, "Direct observation of degenerate two-photon absorption and its saturation in WS_2 and MoS_2 monolayer and few-layer films," ACS nano, vol. 9, pp. 7142-7150, 2015.

[51] H. Wu, R. Yang, B. Song, Q. Han, J. Li, Y. Zhang, Y. Fang, R. Tenne, and C. Wang, "Biocompatible inorganic fullerene-like molybdenum disulfide nanoparticles produced by pulsed laser ablation in water," ACS nano, vol. 5, pp. 1276-1281, 2011.

[52] Y. Shi, Y. Wan, R. Liu, B. Tu, and D. Zhao, "Synthesis of highly ordered mesoporous crystalline WS_2 and MoS_2 via a high-temperature reductive sulfuration route," Journal of the American Chemical Society, vol. 129, pp. 9522-9531, 2007.

[53] H. R. Matte, A. Gomathi, A. K. Manna, D. J. Late, R. Datta, S. K. Pati, and C. Rao, "MoS_2 and WS_2 analogues of graphene," Angewandte Chemie International Edition, vol. 24, pp. 4059-4062, 2010.

[54] L. Ye, C. Wu, W. Guo, and Y. Xie, "MoS_2 hierarchical hollow cubic cages assembled by bilayers: one-step synthesis and their electrochemical hydrogen storage properties," Chemical communications, pp. 4738-4740, 2006.

[55] X. Li and K. Peng, "Hydrothermal synthesis of MoS_2 nanosheet/palygorskite nanofiber hybrid nanostructures for enhanced catalytic activity," Applied Clay Science, vol. 162, pp. 175-181, 2018.

[56] J. S. Roy, G. Dugas, S. Morency, and Y. Messaddeq, "Rapid degradation of Rhodamine B using enhanced photocatalytic activity of MoS_2 nanoflowers under concentrated sunlight irradiation," Physica E: Low-dimensional Systems and Nanostructures, vol. 120, p. 114114, 2020.

[57] C. Sharma, A. K. Srivastava, and M. K. Gupta, "Structural, optical and temperature dependent electric modulus property of few layer MoS_2 nanosheets," Physica B: Condensed Matter, vol. 669, p. 415290, 2023.

[58] R. Sanikop, S. Gautam, K. H. Chae, and C. Sudakar, "Robust ferromagnetism in Mn and Co doped 2D-MoS_2 nanosheets: Dopant and phase segregation effects," Journal of Magnetism and Magnetic Materials, vol. 537, p. 168226, 2021.

[59] Y. Liu, D. Tang, H. Zhong, Q. Zhang, J. Yang, and L. Zhang, "A novel MoS_2/C nanocomposite as an anode material for lithium-ion batteries," Journal of Alloys and Compounds, vol. 729, pp. 583-589, 2017.

[60] D. Nath, F. Singh, and R. Das, "X-ray diffraction analysis by Williamson-Hall, Halder-Wagner and size-strain plot methods of CdSe nanoparticles-a comparative study," Materials Chemistry and Physics, vol. 239, p. 122021, 2020.

[61] G. Kumar, R. Kotnala, J. Shah, V. Kumar, A. Kumar, P. Dhiman, and M. Singh, "Cation distribution: a key to ascertain the magnetic interactions in a cobalt substituted Mg–Mn nanoferrite matrix," Physical Chemistry Chemical Physics, vol. 19, pp. 16669-16680, 2017.

[62] Available from: http://mill2.chem.ucl.ac.uk/tutorial/lmgp/celref.htm

[63] A. El-Fadla, M. Hussiena, A. Soltana, and A. Abu-Sehlya, "Structure, optical and visible-light photocatalytic performance of $Mo_{1-x}Co_xS_2$ ($0\leq x\leq 0.1$) nanoparticles synthesized by facile hydrothermal method for methylene blue dye degradation."

[64] S. Prabhakar Vattikuti, C. Byon, C. Venkata Reddy, B. Venkatesh, and J. Shim, "Synthesis and structural characterization of MoS_2 nanospheres and nanosheets using solvothermal method," Journal of Materials Science, vol. 50, pp. 5024-5038, 2015.

[65] K. Krishnamoorthy, G. K. Veerasubramani, S. Radhakrishnan, and S. J. Kim, "Supercapacitive properties of hydrothermally synthesized sphere like MoS_2 nanostructures," Materials Research Bulletin, vol. 50, pp. 499-502, 2014.

[66] U. K. Sen and S. Mitra, "High-rate and high-energy-density lithium-ion battery anode containing 2D MoS_2 nanowall and cellulose binder," ACS applied materials & interfaces, vol. 5, pp. 1240-1247, 2013.

[67] E. Ghaleghafi, M. B. Rahmani, and Z.-H. Wei, "Photoluminescence and UV photosensitivity of few-layered MoS_2 nanosheets synthesized under different hydrothermal growth times," Journal of Materials Science, vol. 56, pp. 11749-11768, 2021.

[68] G. Nagaraju, C. Tharamani, G. Chandrappa, and J. Livage, "Hydrothermal synthesis of amorphous MoS_2 nanofiber bundles via acidification of ammonium heptamolybdate tetrahydrate," Nanoscale research letters, vol. 2, pp. 461-468, 2007.

[69] P. Sharma, M. K. Singh, and M. S. Mehata, "Sunlight-driven MoS_2 nanosheets mediated degradation of dye (crystal violet) for wastewater treatment," Journal of Molecular Structure, vol. 1249, p. 131651, 2022.

[70] S. P. Vattikuti and C. Byon, "Synthesis and characterization of molybdenum disulfide nanoflowers and nanosheets: nanotribology," Journal of Nanomaterials, vol. 2015, pp. 9-9, 2015.

[71] H. Sadhanala, S. Senapati, K. V. Harika, K. K. Nanda, and A. Gedanken, "Green synthesis of MoS_2 nanoflowers for efficient degradation of methylene blue and crystal violet dyes under natural sun light conditions," New Journal of Chemistry, vol. 42, pp. 14318-14324, 2018.

[72] A. Raza, M. Ikram, M. Aqeel, M. Imran, A. Ul-Hamid, K. N. Riaz, and S. Ali, "Enhanced industrial dye degradation using Co doped in chemically exfoliated MoS_2 nanosheets," Applied Nanoscience, vol. 10, pp. 1535-1544, 2020.

[73] M. Farooq and T. Iqbal, "Facile Hydrothermal Synthesis of Cd Doped MoS_2 Nanomaterials for Degradation of Organic Pollutants: Correlation Between

Experimental and COMSOL Simulation," Journal of Inorganic and Organometallic Polymers and Materials, vol. 32, pp. 4422-4433, 2022.

[74] F. L. Deepak, A. Mayoral, and M. J. Yacaman, "Faceted MoS_2 nanotubes and nanoflowers," Materials Chemistry and Physics, vol. 118, pp. 392-397, 2009.

[75] P. Falcaro, F. Normandin, M. Takahashi, P. Scopece, H. Amenitsch, S. Costacurta, C. M. Doherty, J. S. Laird, M. D. Lay, and F. Lisi, "Dynamic Control of MOF- 5 Crystal Positioning Using a Magnetic Field," Advanced Materials, vol. 23, pp. 3901-3906, 2011.

[76] W. Zhao, Z. Ghorannevis, L. Chu, M. Toh, C. Kloc, P.-H. Tan, and G. Eda, "Evolution of electronic structure in atomically thin sheets of WS_2 and WSe_2," ACS nano, vol. 7, pp. 791-797, 2013.

[77] L. Muscuso, S. Cravanzola, F. Cesano, D. Scarano, and A. Zecchina, "Optical, vibrational, and structural properties of MoS_2 nanoparticles obtained by exfoliation and fragmentation via ultrasound cavitation in isopropyl alcohol," The Journal of Physical Chemistry C, vol. 119, pp. 3791-3801, 2015.

[78] C. Rao, U. Maitra, and U. V. Waghmare, "Extraordinary attributes of 2-dimensional MoS_2 nanosheets," Chemical Physics Letters, vol. 609, pp. 172-183, 2014.

[79] Y. Kim, D. Lee, S. Y. Kim, E. Kang, and C. K. Kim, "Nanocomposite synthesis of nanodiamond and molybdenum disulfide," Nanomaterials, vol. 9, p. 927, 2019.

[80] T. Cassagneau, J. H. Fendler, and T. E. Mallouk, "Optical and electrical characterizations of ultrathin films self-assembled from 11-aminoundecanoic acid capped TiO_2 nanoparticles and polyallylamine hydrochloride," Langmuir, vol. 16, pp. 241-246, 2000.

[81] B. D. Viezbicke, S. Patel, B. E. Davis, and D. P. Birnie III, "Evaluation of the Tauc method for optical absorption edge determination: ZnO thin films as a model system," physica status solidi (b), vol. 252, pp. 1700-1710, 2015.

[82] M. Zhou, L. Cheng, Z. Chen, L. Chen, and Y. Ma, "CdSe QDs@ MoS_2 nanocomposites with enhanced photocatalytic activity towards ceftriaxone sodium degradation under visible-light irradiation," Journal of Alloys and Compounds, vol. 869, p. 159322, 2021.

[83] V. Forsberg, R. Zhang, J. Bäckström, C. Dahlström, B. Andres, M. Norgren, M. Andersson, M. Hummelgård, and H. Olin, "Exfoliated MoS_2 in water without additives," PloS one, vol. 11, p. e0154522, 2016.

[84] S. A. Darsara, M. Seifi, and M. B. Askari, "One-step hydrothermal synthesis of MoS_2/CdS nanocomposite and study of structural, photocatalytic, and optical properties of this nanocomposite," Optik, vol. 169, pp. 249-256, 2018.

[85] X.-J. Lv, W.-F. Fu, C.-Y. Hu, Y. Chen, and W.-B. Zhou, "Photocatalytic reduction of CO_2 with H_2O over a graphene-modified NiO_x–Ta_2O_5 composite photocatalyst: coupling yields of methanol and hydrogen," RSC advances, vol. 3, pp. 1753-1757, 2013.

[86] R. Hidayat, S. Wahyuningsih, G. Fadillah, and A. H. Ramelan, "Highly visible light photodegradation of RhB as synthetic organic dye pollutant over TiO_2-modified reduced graphene oxide," Journal of Inorganic and Organometallic Polymers and Materials, pp. 1-9, 2022.

[87] W. Teng, X. Li, Q. Zhao, J. Zhao, and D. Zhang, "In situ capture of active species and oxidation mechanism of RhB and MB dyes over sunlight-driven Ag/Ag_3PO_4 plasmonic nanocatalyst," Applied Catalysis B: Environmental, vol. 125, pp. 538-545, 2012.

[88] S.-T. Liu, J. Huang, Y. Ye, A.-B. Zhang, L. Pan, and X.-G. Chen, "Microwave enhanced Fenton process for the removal of methylene blue from aqueous solution," Chemical Engineering Journal, vol. 215, pp. 586-590, 2013.

[89] K. V. Kumar, K. Porkodi, and Rocha, "Langmuir–Hinshelwood kinetics–a theoretical study," Catalysis Communications, vol. 9, pp. 82-84, 2008.

[90] Y. Cao, Q. Li, and W. Wang, "Construction of a crossed-layer-structure MoS_2/gC_3N_4 heterojunction with enhanced photocatalytic performance," RSC advances, vol. 7, pp. 6131-6139, 2017.

[91] S. Kumar, N. L. Reddy, H. S. Kushwaha, A. Kumar, M. V. Shankar, K. Bhattacharyya, A. Halder, and V. Krishnan, "Efficient electron transfer across ZnO-MoS_2-RGO heterojunction for remarkably enhanced sunlight driven photocatalytic hydrogen evolution," ChemSusChem, vol. 10, p. 603, 2017.

[92] S. Kumar, V. Sharma, K. Bhattacharyya, and V. Krishnan, "N-doped ZnO–MoS_2 binary heterojunctions: the dual role of 2D MoS_2 in the enhancement of photostability and photocatalytic activity under visible light irradiation for tetracycline degradation," Materials Chemistry Frontiers, vol. 1, pp. 1093-1106, 2017.

[93] S. Kumar, V. Maivizhikannan, J. Drews, and V. Krishnan, "Fabrication of nanoheterostructures of boron doped ZnO-MoS_2 with enhanced photostability and photocatalytic activity for environmental remediation applications," Vacuum, vol. 163, pp. 88-98, 2019.